



Article

Chalcogenide Quaternary $\text{Cu}_2\text{FeSnS}_4$ Nanocrystals for Solar Cells: Explosive Character of Mechanochemical Synthesis and Environmental Challenge

Peter Baláž¹, Matej Baláž^{1,*} , María J. Sayagués², Alexander Eliyas³ , Nina G. Kostova³, Mária Kaňuchová⁴, Erika Dutková⁴ and Anna Zorkovská¹

¹ Institute of Geotechnics, Slovak Academy of Sciences, 040 01 Košice, Slovakia; balaz@saske.sk (P.B.); dutkova@saske.sk (E.D.); zorkovska.anna@gmail.com (A.Z.)

² Institute of Materials Science of Seville (CSIC-US), 410 92 Sevilla, Spain; mjsayagues@icmse.csic.es

³ Institute of Catalysis, Bulgarian Academy of Sciences, 1113 Sofia, Bulgaria; alel@ic.bas.bg (A.E.); nkostova@ic.bas.bg (N.G.K.)

⁴ Faculty of Mining, Ecology, Process Control and Geotechnologies, Technical University of Košice, 042 00 Košice, Slovakia; maria.kanuchova@tuke.sk

* Correspondence: balazm@saske.sk; Tel.: +421-55-792-2603

Academic Editor: Franziska Emmerling

Received: 30 October 2017; Accepted: 5 December 2017; Published: 9 December 2017

Abstract: In this study we demonstrate the synthesis of quaternary semiconductor nanocrystals of stannite $\text{Cu}_2\text{FeSnS}_4$ /rhodostannite $\text{Cu}_2\text{FeSn}_3\text{S}_8$ (CFTS) via mechanochemical route using Cu, Fe, Sn and S elements as precursors in one-pot experiments. Methods of X-ray diffraction (XRD), nitrogen adsorption, high-resolution transmission electron microscopy (HRTEM), scanning transmission electron microscopy (STEM), energy-dispersive X-ray spectroscopy (EDX) and X-ray photoelectron spectroscopy (XPS) were applied to characterize properties of the unique nanostructures. Mechanochemical route of synthesis induced new phenomena like explosive character of reaction, where three stages could be identified and the formation of nanostructures 5–10 nm in size. By using XPS method, Cu(I), Fe(II), Sn(IV) and S(-II) species were identified on the surface of CFTS. The value of optical band gap 1.27 eV is optimal for semiconductors applicable as absorbers in solar cells. The significant photocatalytic activity of the CFTS nanocrystals was also evidenced. The obtained results confirm the excellent properties of the quaternary semiconductor nanocrystals synthesized from earth-abundant elements.

Keywords: stannite; semiconductor; nanostructure; photocatalysis; mechanochemistry; explosion

1. Introduction

Photovoltaic materials directly converting solar energy into electricity represent an urgent challenge nowadays. They reflect today's increasing global energy demand [1]. As a logical consequence, there is a permanent activity in photovoltaic research. The main focus is to substitute silicon-based photovoltaic cells (the first generation of materials), which is efficient but costly, by the second generation of materials, such as CdTe and $\text{CuIn}_{1-x}\text{Ga}_x\text{Se}_2$ (CIGS), which possess good power conversion efficiency and stability and are cheaper to produce [2,3]. However, these materials represent an environmental problem because of cadmium and selenium toxicity, limited availability and high price of indium and gallium [2,4,5]. The research into earth-abundant, environmentally sustainable and cheap analogues is therefore fully justified. The main focus is on kesterite $\text{Cu}_2\text{ZnSnS}_4$ (CZTS) quaternary crystals, which emerged as potential candidates [5–12].

The mechanochemical synthesis as a version of solid-state approach has been applied for various materials [13–20]. The combination of mechanical alloying and spark plasma sintering has documented the possibility to synthesize high-performance thermoelectric materials with the possibility to scale the synthesis process. While CZTS has been already synthesized by a mechanochemical route in 2011 [21] and plenty of papers on this topic have emerged [22–29], literature on $\text{Cu}_2\text{FeSn}_3\text{S}_8$ (CFTS) mechanochemical synthesis is rather scarce. In 2014, an attempt was published to apply mechanochemistry for the synthesis of CFTS [23]. However, milling has been applied only for homogenization of reaction mixture and the synthesis process was carried out subsequently at 400 °C for eight hours in argon atmosphere. The only two papers reporting CFTS mechanochemical synthesis are by the authors of this work [30,31]. The authors studied the kinetics of mechanochemical synthesis and magnetic properties of the prepared nanocrystals.

In this paper, we apply the solid state approach to synthesize stannite $\text{Cu}_2\text{FeSnS}_4$ (CFTS) nanocrystals, which represent an analogue to CZTS. The aim and novelty of the present paper is to elucidate the explosive character of mechanochemical synthesis and the photocatalytic properties of optimal CFTS sample. The surface composition of the CFTS nanocrystals is studied also for the first time.

2. Methods

The starting elements copper (99%, Merck, Germany), iron (99%, Merck, Germany), tin (99.9%, Merck, Germany) and sulfur (CG Chemikalien, Germany) were weighed and mixed in atomic ratio of 2:1:1:4 according to stoichiometry $\text{Cu}_2\text{FeSnS}_4$.

The starting mixture was subjected to milling in a high-energy planetary mill Pulverisette 7 (Fritsch, Idar-Oberstein, Germany) in order to prepare nanocrystalline quaternary semiconductor stannite $\text{Cu}_2\text{FeSnS}_4$ (further CFTS). The mill worked under the following conditions: loading 18 balls (diameter 10 mm) of tungsten carbide, milling pot of tungsten carbide and volume 80 mL, total weight of starting mixture 2 g, ball-to-powder ratio 70:1, milling speed 500 min^{-1} , milling time 120 min, milling atmosphere air. The milling was stopped after 60 min. of milling, in order to avoid overheating. The break took 30 min. The mill has been applied in combination with a GTM system (Fritsch, Idar-Oberstein, Germany) in order to pursue changes in pressure and temperature during milling.

The crystalline structure was characterized using a D8 Advance X-ray diffractometer (Bruker, Karlsruhe, Germany) in the Bragg-Brentano geometry, working with a $\text{CuK}\alpha$ ($\lambda = 0.15406$ nm) radiation and a scintillation detector. The data were collected over the angular range $10^\circ < 2\theta < 100^\circ$ with scanning steps of 0.020 and the measurement step time interval of 6 s. For the data processing, the commercial Bruker tools have been used. Namely, for the phase identification, the Diffracplus Eva and the ICDD PDF2 database and for Rietveld analysis, the Diffracplus Topas software (Bruker, Karlsruhe, Germany) have been applied.

A nitrogen adsorption apparatus NOVA 1200e Surface Area Pore Size Analyzer (Quantachrome Instruments, Hartley Wintney, Great Britain) was employed to record the nitrogen adsorption–desorption isotherms at the temperature of liquid nitrogen. The specific surface area was calculated using the Brunauer–Emmet–Teller (BET) equation. The pore size distribution was calculated using Barret–Joyner–Halenda (BJH) method.

The absorption spectrum was measured using a UV–Vis spectrophotometer Helios Gamma (Thermo Electron Corporation, Cambridge, Great Britain) in a quartz cell by dispersing the synthesized nanoparticles in absolute ethanol by ultrasonic stirring.

A FEG high-resolution transmission electron-microscope (HRTEM) model Tecnai G2F30 S-twin (FEI Company, Oxford, MS, USA) with the scanning-transmission capabilities (STEM) was also used. The measurements were conducted at 300 kV with 0.2 nm point resolution. The microscope is equipped with a high angle annular dark field (HAADF) detector of 0.16 nm point resolution (Fischione Instruments, Corporate Circle Export, PA, USA), and an INBCA ZX-max 80 silicon drift detector (SDD) for the energy-dispersive X-ray analysis (EDX). The GHR micrograph analysis, lattice spacing, First

Fourier Transform (FFT) and phase interpretation was done with the Gatan micrograph software (Gatan Inc., Pleasanton, CA, USA) and the Java version of the Electron Microscope Software JEM (Pittsburgh, PA, USA). The analysis of HAAD STEM images and the EDX spectra profile were conducted with the ES Vision software (FEI Company, Oxford, MS, USA).

XPS measurements were performed using XPS instrument SPECS (SPECS GmbH, Berlin, Germany) equipped with PHOIBOS 100 SCD and non-monochromatic X-ray source. The survey surface spectrum was measured at 70 eV transition energy and core spectra at 20 eV at room temperature. All the spectra were acquired at a basic pressure of 1×10^{-8} mbar with AlK_{α} excitation at 10 kV (200 W). The data were analysed by SpecsLab2 CasaXPS software (Casa Software Ltd., Teignmouth, Great Britain). A Shirley and Tougaard type of baseline was used for all peak fits. The spectrometer was calibrated against silver (Ag 3d). All samples showed variable degrees of charging due to their insulating nature. The problem was resolved by the calibration on carbon.

The photocatalytic activity experiments were carried out using a semi-batch photocatalytic reactor equipped with an electromagnetic stirrer (1250 rpm), similarly as in our previous work [32]. The activity was evaluated using UV-C light of intensity 0.05 W/cm^2 , measured by Cole Parmer radiometer (Vernon Hills, IL, USA) Model VLX-3.W, equipped with CX-254 sensor for 254 nm wavelength. The suspensions were prepared by adding 100 mg of the CFTS sample to 100 mL of the azo dye Chromium Acidic Black 194 (CAB) aqueous solution with a concentration of 1×10^{-3} M. The course of the photocatalytic oxidation reaction was monitored by estimating the degree of CAB discoloring based on absorbance measured by a CamSpec (Cambridge Spectrophotometers Co., Cambridge, United Kingdom) model M501 Single Beam scanning UV/Visible Spectrophotometer (wavelength range 190–1100 nm). The extinction (absorbance) E_0 of the diluted solution was measured at the wavelength of its maximum in the visible spectrum $\lambda_{\text{max}} = 570 \text{ nm}$ to determine (based on the previous calibration of spectrophotometer) the exact concentration $C_0 = 48.9 \text{ ppm}$ ($E_0 = 0.674 \text{ Abs.}$). The total conversion degree, ϵ_t was calculated by the formula

$$\epsilon_t(\%) = \frac{C_0 - C_t}{C_0} \cdot 100 \quad (1)$$

where C_t is the residual concentration of CAB in time t .

3. Results and Discussion

3.1. Explosive Character of Synthesis

The mechanochemical synthesis of the quaternary sulfides is always challenging, and the possible interaction between elemental precursors can proceed in different manners, depending e.g., on the morphologies of used metals. A possible explosive reaction between Cu and S should have taken place, as the same elemental precursors as in paper [33] were used. However, in this case, the explosion documented by a sharp pressure increase could possibly not be evidenced, because there was quite a large number of other elements present. The kinetics of the synthesis of CFTS phase was already described in [31], where it was found out that the reaction proceeds through the formation of CuS, and then continues with consumption of tin, and iron is embedded into the structure as the last element. Based on this, possible reactions stages can be distinguished, although the milling was performed in different mill in that case. However, the results provided therein, in combination with pursuing of pressure and temperature in the milling chamber, can give us at least some idea about the processes taking place. The gas pressure and temperature changes with respect to milling time are presented in Figure 1.

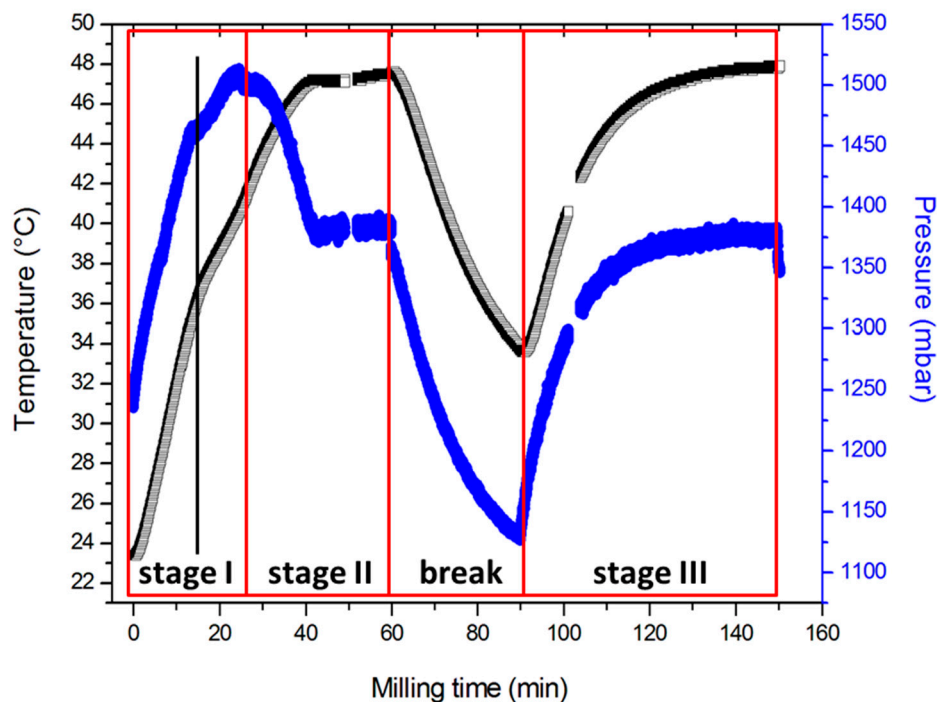


Figure 1. Gas pressure and temperature changes in the milling chamber during $\text{Cu}_2\text{FeSn}_4/\text{Cu}_2\text{FeSn}_3\text{S}_8$ (CFTS) synthesis and possible reaction stages.

Upon the start of the reaction, both pressure and temperature sharply increase. The first interesting phenomenon was observed after approximately 16 min of milling (marked by black line in Figure 1), when the slope of the pressure and temperature curve increase slightly changes and after this point, both parameters increase less rapidly. This point is also associated with the start of a scraping sound in the mill, which can be heard during the rest of milling. We hypothesize that this is a result of the exothermic reaction taking place between Sn and CuS, as the latter should be definitely formed after this time of milling [33]. It has to be noted that the rapid consumption of tin was also documented in the synthesis of CZTS nanocrystals, despite the fact that the reaction proceeded more-or-less in a gradual manner until that point [24]. The maximum pressure (1513 mbar) was evidenced after 25 min of milling. Based on the data in [31], we hypothesize that the formation of CuS, and also incorporation of Sn, most probably with the formation of mohite Cu_2SnS_3 structure, should all take place within this stage (stage I). When the maximum pressure is reached, it can be seen that the temperature still increases. This is most probably because in this experimental setup, pressure is more sensitive parameter to be observed than temperature. The pressure in the chamber then starts to decrease, and stage II of the reaction starts. In this stage, only the incorporation of iron in a gradual manner to form final structures of stannite and rhodostannite takes place. The pressure drops down to a value around 1380 mbar and this value slightly increases until 60 min of milling. This increase is a consequence of energy accumulation during milling. Regarding temperature, its value around 47 °C was reached after approximately 45 min from the start of milling and increased only very slightly till 60 min. The milling was then stopped for 30 min in order to avoid overheating and both pressure and temperature significantly decrease during this period; however, when the milling is re-started, they increase quite rapidly again and reach the value which was achieved prior to the break approximately in 15 min after the re-start. During this stage, most probably only stannite-rhodostannite transformation is taking place, and probably residual iron can react to form CFTS. To conclude this section, it seems that synthesis of CFTS is accompanied with more phenomena, which contribute to the changes in pressure in the milling chamber and only demonstrate the complexity of this system.

3.2. Structural Properties

In Figure 2 the XRD pattern obtained after milling of the Cu, Fe, Sn and S precursor powders is given. No elemental precursors are visible after milling for 120 min. All the peaks can be assigned to stannite $\text{Cu}_2\text{FeSnS}_4$ (JCPDS 44-1476) and rhodostannite $\text{Cu}_2\text{FeSn}_3\text{S}_8$ (JCPDS 88-0378). Both compounds are tetragonal. The XRD pattern exhibits a complex of peaks with the three most intensive ones corresponding to (112), (204) and (312) planes of the tetragonal nanocrystals. More complex elucidation of the XRD data has been performed in our previous paper [30].

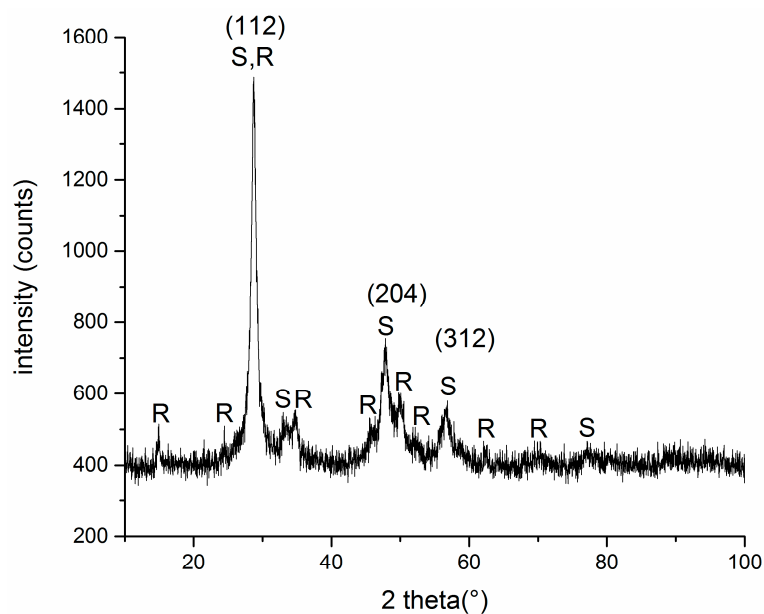


Figure 2. XRD pattern of the CFTS sample. R: rhodostannite $\text{Cu}_2\text{FeSn}_3\text{S}_8$; S: stannite $\text{Cu}_2\text{FeSnS}_4$.

3.3. Microstructural Properties

CFTS sample after milling is formed by agglomerated nanoparticles as it is shown in the TEM micrograph (Figure 3a). The corresponding characteristic ED inset is formed by rings due to the small coherent diffraction domains (10–20 nm). All of them were indexed in the tetragonal system of the $\text{Cu}_2\text{FeSnS}_4$ (1–42 m space group) and $\text{Cu}_2\text{FeSn}_3\text{S}_8$ (141/a space group) compounds and the planes are marked. These data are in agreement with the X-ray diffraction results. Around the agglomerated particles, very small isolated nanoparticles were found, as it is shown in the TEM and STEM micrographs presented in Figure 3b,c. These nanoparticles show square-faceted shape with a bimodal character. Some nanocrystals are faceted and very small (5–10 nm) with square and elongated shape (insets of Figure 3b) and others form a kind of fractal structure.

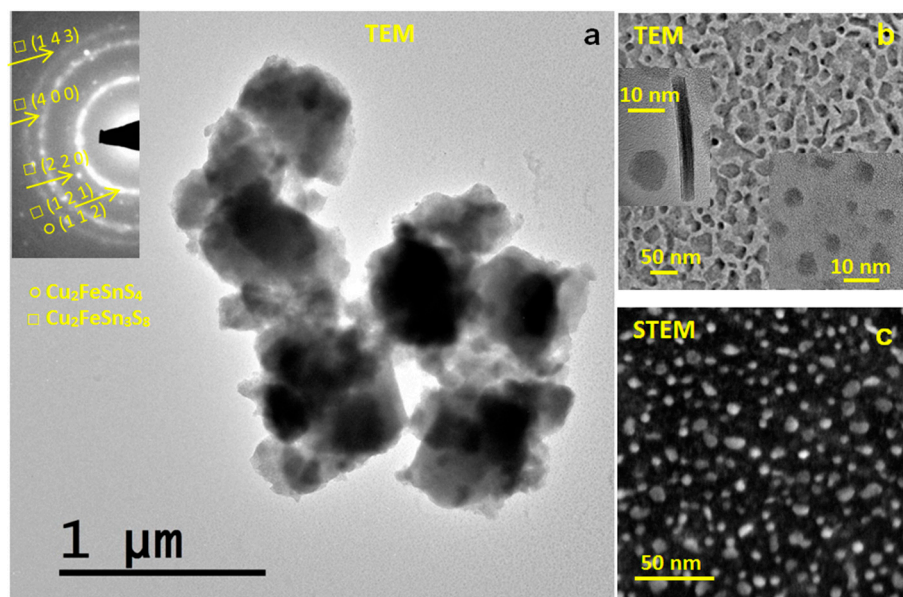


Figure 3. Microcharacterization of the CFTS sample: (a) TEM image of the agglomerated particles and the corresponding ED pattern (inset), (b) TEM image of the isolated particles and regions with tiny crystallites and elongated particles are in inset, (c) STEM image of isolated particles.

The high resolution TEM images of the agglomerated areas show that the sample is formed by very small crystallites (Figure 4a–c). Some oriented crystallites (marked in yellow square) and the corresponding first Fourier transform (FFT) are depicted in the insets. The analysis of the reciprocal spacings in the FFT allows us to distinguish which is the crystalline phase and the (h k l) planes are marked. $\text{Cu}_2\text{FeSnS}_4$ and $\text{Cu}_2\text{FeSn}_3\text{S}_8$ phases were found in the sample. Two $\text{Cu}_2\text{FeSnS}_4$ crystallites oriented along the [1 2 3] and [3 5 1] zone axes (Figure 4a,b, respectively) and $\text{Cu}_2\text{FeSn}_3\text{S}_8$ oriented along the [3 7 1] direction (Figure 4c) are depicted for the sample.

High resolution TEM micrographs of the isolated nanoparticles show that many of them are $\text{Cu}_2\text{FeSnS}_4$ and $\text{Cu}_2\text{FeSn}_3\text{S}_8$ crystals and [111] direction of $\text{Cu}_2\text{FeSnS}_4$ is shown in Figure 4d. However, some isolated nanocrystals that could be indexed in neither of those two phases were also found. This fact, together with the compositional analysis results indicate that some other minor phases could have formed.

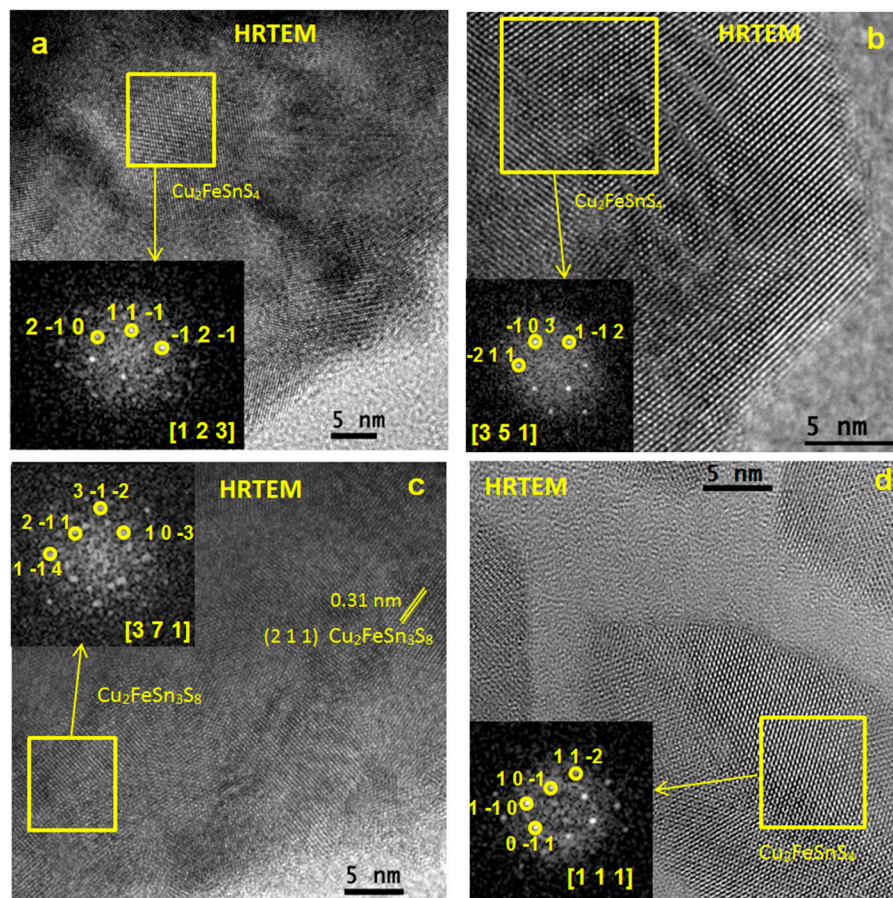


Figure 4. High-resolution TEM images of the CFTS sample: Micrographs of (a–c) agglomerated nanocrystals and (d) isolated crystallite. The yellow squares show oriented crystallites of both phases and the corresponding FFT are depicted in the insets.

3.4. Optical Properties

The optical properties of the synthesized CFTS nanocrystals were investigated using UV–Vis absorption spectroscopy. Figure 5 shows the obtained spectrum with a broad absorption in the visible range of wavelength. The optical band gap energy of the CFTS sample was determined by plotting $(\alpha h\nu)^2$ as a function of the photon energy ($h\nu$) and extrapolating the linear portion of the spectrum in the band edge region, as it is displayed in the inset of Figure 5. The band gap energy was calculated by a procedure described in paper [30]. The obtained value 1.27 eV is acceptable for absorbers in solar cells [34,35].

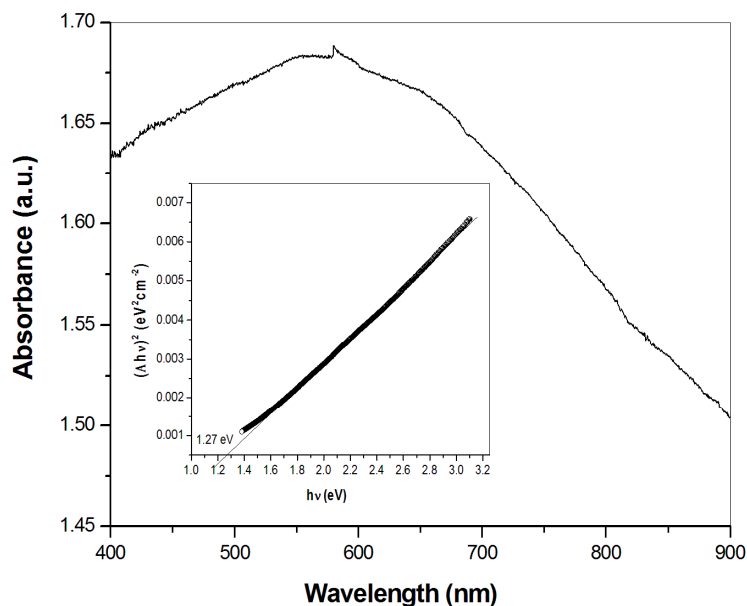


Figure 5. UV-Vis absorption spectrum of the CFTS sample and corresponding Tauc plot (inset).

3.5. Surface Properties

The specific surface area for this sample was determined as $6.1 \text{ m}^2 \cdot \text{g}^{-1}$, which is quite a high value in comparison with that of various sulfides, which were synthesized by a mechanochemical approach previously [36]. Regarding stannite, we obtained a slightly higher value compared to that presented in our previous paper ($3.5 \text{ m}^2 \cdot \text{g}^{-1}$) [30], in which the sample was prepared in P6 mill with slightly higher ball-to-powder ratio, which could lead to more intensive agglomeration. Also the different conditions of milling could influence the value. Regarding the kinetic study [31], the values up to $5.5 \text{ m}^2 \cdot \text{g}^{-1}$ were obtained until 45 min of milling in P6 mill. Of course, if a different technique is applied for the synthesis of CFTS, a mesoporous structure with higher S_{BET} value can be obtained [37]. Quite a high specific surface area could possibly also contribute to the photocatalytic activity of this material (see Section 3.6).

X-ray photoelectron spectroscopy was used to elucidate the surface composition of as-synthesized CFTS nanocrystals, as it is shown in Figure 6. Figure 6a shows that the most intensive Cu binding peaks were located at 934.4 eV and 952.3 eV. The peak splitting of 17.9 eV indicates Cu(I) configuration [38,39]. However, the satellite peak at 943.8 eV documents also the presence of a small amount of copper in Cu(II) configuration. The most prevailing peaks at 710.0 eV and 723.7 eV (Figure 6b) can be assigned to Fe(II) configuration, which corresponds to reported values in literature for CFTS phase [38,40,41]. XPS spectrum of tin in Figure 6c with peaks at 487.4 eV and 496.6 eV documents the presence of Sn(IV) configuration [38,39]. Finally, in Figure 6d, high-resolution spectrum for sulfur is given. The solo peak at 163.5 eV is the evidence of S(-II) configuration [39] and it is in accord with the 160–164 eV range expected for S in sulfide phases [38]. The values of binding energies indicate that the four elements are in Cu(I), Fe(II), Sn(IV) and S(-II) oxidation states, which was also documented in other works where non-mechanochemical approach for synthesis of CFTS has been applied [34,35,37,42–44].

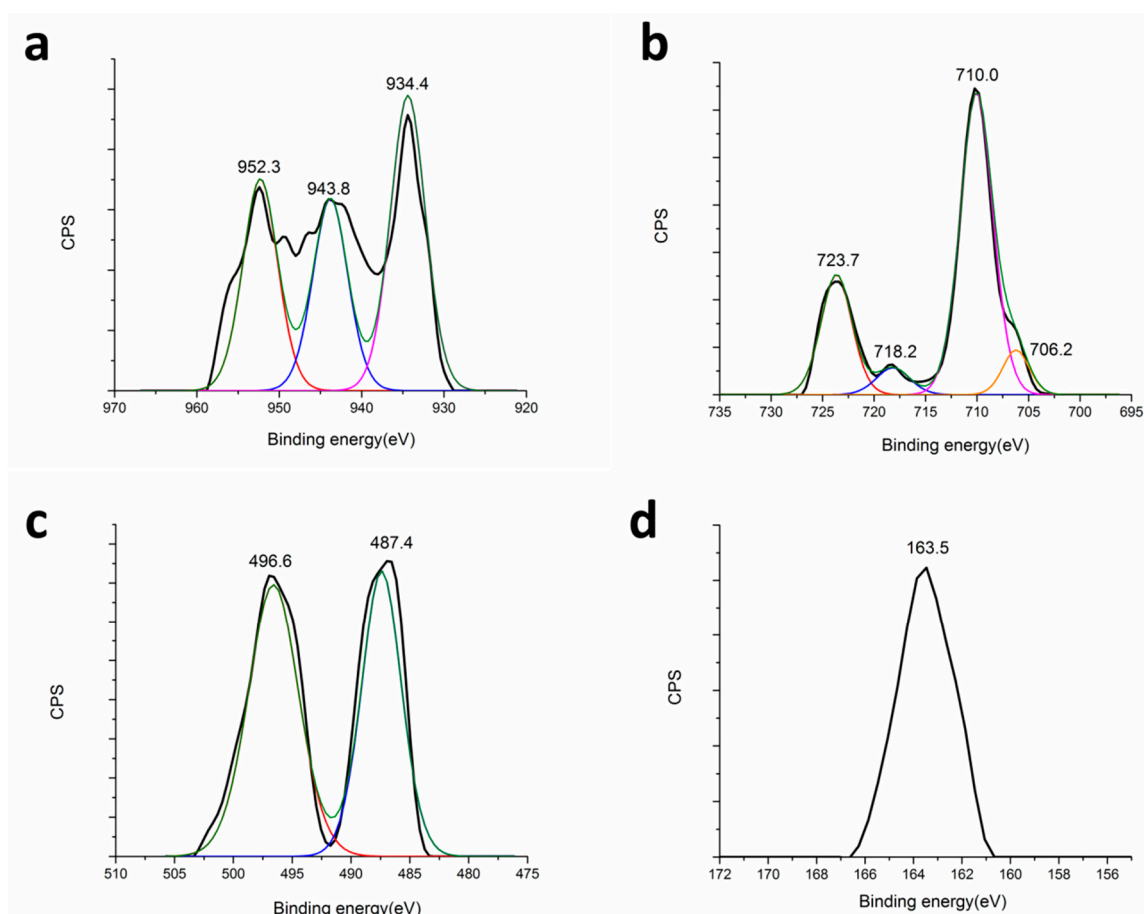


Figure 6. High-resolution XPS spectra of the CFTS sample: (a)- Cu 2p, (b)- Fe 2p, (c)- Sn 3d, (d)- S 2p.

3.6. Photocatalytic Activity

Data on photocatalytic degradation of Methylene Blue in the presence of kesterite $\text{Cu}_2\text{ZnSnS}_4$ can be found in recent literature [45–48]. However, the photocatalytic activity of the synthesized stannite $\text{Cu}_2\text{FeSnS}_4$ sample is here studied for the first time. The optical absorption experiments of the model organic azo dye Chromium Acidic Black 194 (CAB) decomposition with respect to the illumination time were performed. Using UV-C light of intensity $0.05 \text{ W}\cdot\text{cm}^{-2}$ and illumination times 60, 120 and 180 min, the values of the CAB photocatalytic destruction 15.9%, 17.6% and 20.8%, respectively, were obtained. For comparison, Zhou et al. [46] documented that $\text{Cu}_2\text{ZnSnS}_4$ nanoparticles degraded 30% Methylene Blue in 240 min. The results illustrate the promising potential of CFTS utilization for the treatment of toxic organic components. In principle, their abundance in the vicinity of solar cells with quaternary semiconductor nanocrystals such as CFTS cannot be dropped out.

4. Conclusions

In this work, the simple mechanochemical solid-state synthesis of stannite $\text{Cu}_2\text{FeSnS}_4$ from elemental precursors has been demonstrated. Simultaneously, rhodostannite $\text{Cu}_2\text{FeSn}_3\text{S}_8$ was detected among the reaction products. Both compounds are tetragonal with the presence of nanostructures of 5–10 nm in size. As a new phenomenon, the explosive character of synthesis has been evidenced. The reaction exhibits a multistage character, most probably proceeding via CuS and Cu_2SnS_3 , as was discussed in relation with temperature and pressure changes in the milling pot. The optical band gap 1.27 eV determined from UV-Vis absorption data using Tauc plot is in harmony with the values required for solar cell absorbers. The study of photocatalytic activity of the synthesized nanocrystals revealed further environmental potential of CFTS for the treatment of toxic organic pollutants. Finally,

the applied mechanochemical synthesis procedure represents a promising way to produce nanocrystals for large-scale applications.

Acknowledgments: This work was supported by the Slovak Research and Development Agency APVV (project APVV-0103-14) and by the National Science Fund (Bulgaria) under the contract DNTS/Slovakia 01/2. The support of the Research excellence centre on earth sources, extraction and treatment - 2nd phase supported by the Research & Development Operational Programme funded by the ERDF No. 26220120038 is also gratefully acknowledged.

Author Contributions: Peter Baláž proposed an idea of mechanochemical synthesis and coordinated the action. Matej Baláž performed the milling experiments in explosive mode and nitrogen adsorption measurements. Alexander Eliyas and Nina G. Kostova performed the photocatalytic experiments. María J. Sayagués and Anna Zorkovská performed the structural analysis. Erika Dutková performed optical measurements and Mária Kaňuchová realized the XPS measurements. All authors read and approve the final manuscript.

Conflicts of Interest: The authors declare that they have no competing conflicts of interests.

References

1. Polman, A.; Knight, M.; Garnett, E.C.; Ehrler, B.; Sinke, W.C. Photovoltaic materials: Present efficiencies and future challenges. *Science* **2016**, *352*, aad4424. [CrossRef] [PubMed]
2. Delbos, S. Kesterite thin films for photovoltaics: A review. *EPJ Photovolt.* **2012**, *3*, 35004. [CrossRef]
3. Hughes, E. The Next Generation. Available online: <https://www.chemistryworld.com/feature/the-next-generation/1010134.article> (accessed on 30 October 2017).
4. Guo, Q.; Ford, G.M.; Yang, W.C.; Walker, B.C.; Stach, E.A.; Hillhouse, H.W.; Agrawal, R. Fabrication of 7.2% efficient CZTSSe solar cells using CZTS nanocrystals. *J. Am. Chem. Soc.* **2010**, *132*, 17384–17386. [CrossRef] [PubMed]
5. Song, X.B.; Ji, X.; Li, M.; Lin, W.D.; Luo, X.; Zhang, H. A review on development prospect of CZTS based thin film solar cells. *Int. J. Photoenergy* **2014**, *2014*, 613173. [CrossRef]
6. Scragg, J.J. *Copper Zinc Tin Sulfide Thin Films for Photovoltaics*; Springer: Berlin/Heidelberg, Germany, 2011.
7. Siebentritt, S.; Schorr, S. Kesterites — A challenging material for solar cells. *Prog. Photovolt.* **2012**, *20*, 512–519. [CrossRef]
8. Shin, B.; Gunawan, O.; Zhu, Y.; Bojarczuk, N.A.; Chey, S.J.; Guha, S. Thin film solar cell with 8.4% power conversion efficiency using an earth-abundant Cu₂ZnSnS₄ absorber. *Prog. Photovolt.* **2013**, *21*, 72–76. [CrossRef]
9. Hamanaka, Y.; Oyaizu, W.; Kawase, M.; Kuzuya, T. Synthesis of highly non-stoichiometric Cu₂ZnSnS₄ nanoparticles with tunable bandgaps. *J. Nanopart. Res.* **2016**, *19*, 9. [CrossRef]
10. Regulacio, M.D.; Ye, C.; Lim, S.H.; Bosman, M.; Ye, E.; Chen, S.D.; Xu, Q.H.; Han, M.Y. Colloidal nanocrystals of wurtzite-type Cu₂ZnSnS₄: Facile noninjection synthesis and formation mechanism. *Chem. Eur. J.* **2012**, *18*, 3127–3131. [CrossRef]
11. Regulacio, M.D.; Han, M.Y. Multinary I-III-VI₂ and I₂-II-IV-VI₄ semiconductor nanostructures for photocatalytic applications. *Acc. Chem. Res.* **2016**, *49*, 511–519. [CrossRef] [PubMed]
12. Fan, C.M.; Regulacio, M.D.; Ye, C.; Lim, S.H.; Lua, S.K.; Xu, Q.H.; Dong, Z.; Xu, A.W.; Han, M.Y. Colloidal nanocrystals of orthorhombic Cu₂ZnGeS₄: Phase-controlled synthesis, formation mechanism and photocatalytic behavior. *Nanoscale* **2015**, *7*, 3247–3253. [CrossRef]
13. Baláž, P. *Mechanochemistry in Nanoscience and Minerals Engineering*; Springer: Berlin/Heidelberg, Germany, 2008.
14. Baláž, P.; Achimovičová, M.; Baláž, M.; Billik, P.; Cherkezova-Zheleva, Z.; Criado, J.M.; Delogu, F.; Dutková, E.; Gaffet, E.; Gotor, F.J.; et al. Hallmarks of mechanochemistry: From nanoparticles to technology. *Chem. Soc. Rev.* **2013**, *42*, 7571–7637. [CrossRef] [PubMed]
15. Chen, K.; Du, B.; Bonini, N.; Weber, C.; Yan, H.; Reece, M.J. Theory-guided synthesis of an eco-friendly low-cost copper based sulfide thermoelectric material. *J. Phys. Chem. C* **2016**, *120*, 27135–27140. [CrossRef]
16. Du, B.L.; Zhang, R.Z.; Chen, K.; Mahajan, A.; Reece, M.J. The impact of lone-pair electrons on the lattice thermal conductivity of the thermoelectric compound CuSbS₂. *J. Mater. Chem. A* **2017**, *5*, 3249–3259. [CrossRef]
17. Zhang, R.Z.; Chen, K.; Du, B.; Reece, M.J. Screening for Cu-S based thermoelectric materials using crystal structure features. *J. Mater. Chem. A* **2017**, *5*, 5013–5019. [CrossRef]

18. Barbier, T.; Rollin-Martinet, S.; Lemoine, P.; Gascoin, F.; Kaltzoglou, A.; Vaqueiro, P.; Powell, A.V.; Guilmeau, E. Thermoelectric materials: A new rapid synthesis process for nontoxic and high-performance tetrahedrite compounds. *J. Am. Ceram. Soc.* **2016**, *99*, 51–56. [[CrossRef](#)]
19. Kumar, V.P.; Paradis-Fortin, L.; Lemoine, P.; Caignaert, V.; Raveau, B.; Malaman, B.; Le Caër, G.; Cordier, S.; Guilmeau, E. Designing a thermoelectric copper-rich sulfide from a natural mineral: Synthetic germanite $\text{Cu}_{22}\text{Fe}_8\text{Ge}_4\text{S}_{32}$. *Inorg. Chem.* **2017**, *56*, 13376–13381. [[CrossRef](#)] [[PubMed](#)]
20. Kumar, V.P.; Barbier, T.; Caignaert, V.; Raveau, B.; Daou, R.; Malaman, B.; Le Caër, G.; Lemoine, P.; Guilmeau, E. Copper hyper-stoichiometry: The key for the optimization of thermoelectric properties in stannoidite $\text{Cu}_{8+x}\text{Fe}_{3-x}\text{Sn}_2\text{S}_{12}$. *J. Phys. Chem. C* **2017**, *121*, 16454–16461. [[CrossRef](#)]
21. Wang, Y.; Gong, H. $\text{Cu}_2\text{ZnSnS}_4$ synthesized through a green and economic process. *J. Alloys Compd.* **2011**, *509*, 9627–9630. [[CrossRef](#)]
22. Gao, F.; Yamazoe, S.; Maeda, T.; Nakanishi, K.; Wada, T. Structural and optical properties of in-free $\text{Cu}_2\text{ZnSn}(\text{S},\text{Se})_4$ solar cell materials. *Jpn. J. Appl. Phys.* **2012**, *51*, 10NC29. [[CrossRef](#)]
23. Mokurala, K.; Bhargava, P.; Mallick, S. Single step synthesis of chalcogenide nanoparticles $\text{Cu}_2\text{ZnSnS}_4$, $\text{Cu}_2\text{FeSnS}_4$ by thermal decomposition of metal precursors. *Mater. Chem. Phys.* **2014**, *147*, 371–374. [[CrossRef](#)]
24. Park, B.I.; Hwang, Y.; Lee, S.Y.; Lee, J.S.; Park, J.K.; Jeong, J.; Kim, J.Y.; Kim, B.; Cho, S.H.; Lee, D.K. Solvent-free synthesis of $\text{Cu}_2\text{ZnSnS}_4$ nanocrystals: A facile, green, up-scalable route for low cost photovoltaic cells. *Nanoscale* **2014**, *6*, 11703–11711. [[CrossRef](#)] [[PubMed](#)]
25. Shyju, T.S.; Anandhi, S.; Suriakarthick, R.; Gopalakrishnan, R.; Kuppusami, P. Mechanochemical synthesis, deposition and characterization of CZTS and CZTSe materials for solar cell applications. *J. Solid State Chem.* **2015**, *227*, 165–177. [[CrossRef](#)]
26. Ritscher, A.; Just, J.; Dolotko, O.; Schorr, S.; Lerch, M. A mechanochemical route to single phase $\text{Cu}_2\text{ZnSnS}_4$ powder. *J. Alloys Compd.* **2016**, *670*, 289–296. [[CrossRef](#)]
27. Pareek, D.; Balasubramaniam, K.R.; Sharma, P. Reaction pathway for synthesis of $\text{Cu}_2\text{ZnSn}(\text{S}/\text{Se})_4$ via mechano-chemical route and annealing studies. *J. Mater. Sci. Mater. Electron.* **2016**, *28*, 1199–1210. [[CrossRef](#)]
28. Quennet, M.; Ritscher, A.; Lerch, M.; Paulus, B. The order-disorder transition in $\text{Cu}_2\text{ZnSnS}_4$: A theoretical and experimental study. *J. Solid State Chem.* **2017**, *250*, 140–144. [[CrossRef](#)]
29. Liu, C.Q.; Wen, B.; Wang, N.; Liu, S.M.; Wang, H.L.; Jiang, W.W.; Ding, W.Y.; Xu, S.C.; Chai, W.P. Phase evolution and sintering behaviors of $\text{Cu}_2\text{ZnSnS}_4$ powders synthesized by mechanochemical process with different milling parameters. *J. Alloys Compd.* **2017**, *708*, 428–436. [[CrossRef](#)]
30. Baláž, P.; Baláž, M.; Sayagués, M.J.; Škorvánek, I.; Zorkovská, A.; Dutková, E.; Briančin, J.; Kováč, J., Jr.; Kováč, J.; Shpotyuk, Y. Mechanochemical solvent-free synthesis of quaternary semiconductor Cu-Fe-Sn-S nanocrystals. *Nanoscale Res. Lett.* **2017**, *12*, 256–266. [[CrossRef](#)] [[PubMed](#)]
31. Baláž, P.; Baláž, M.; Zorkovská, A.; Škorvánek, I.; Bujňáková, Z.; Trajić, J. Kinetics of solid-state synthesis of quaternary $\text{Cu}_2\text{ZnSnS}_4$ (stannite) nanocrystals for solar energy applications. *Acta Phys. Pol. A* **2017**, *131*, 1153–1155. [[CrossRef](#)]
32. Kostova, N.G.; Achimovičová, M.; Eliyas, A.; Stoyanova, V.; Shopska, M.; Velinov, N.; Baláž, P. Structural and photocatalytic properties of mechanochemically synthesized nanosized ferrite. *Nanosci. Nanotechnol.* **2012**, *12*, 52–55.
33. Baláž, M.; Zorkovská, A.; Urakaev, F.; Baláž, P.; Briančin, J.; Bujňáková, Z.; Achimovičová, M.; Gock, E. Ultrafast mechanochemical synthesis of copper sulfides. *RSC Adv.* **2016**, *6*, 87836–87842. [[CrossRef](#)]
34. Guan, H.; Shen, H.L.; Jiao, B.X.; Wang, X. Structural and optical properties of $\text{Cu}_2\text{ZnSnS}_4$ thin film synthesized via a simple chemical method. *Mater. Sci. Semicond. Process.* **2014**, *25*, 159–162. [[CrossRef](#)]
35. Zhou, B.B.; Yan, X.N.; Li, P.; Yang, L.B.; Yu, D.Y. Raman spectroscopy as a superior tool to understand the synthetic pathway of $\text{Cu}_2\text{ZnSnS}_4$ nanoparticles. *Eur. J. Inorg. Chem.* **2015**, *2015*, 2690–2694. [[CrossRef](#)]
36. Baláž, P. *Extractive Metallurgy of Activated Minerals*; Elsevier: Amsterdam, Netherland, 2000.
37. Ai, L.H.; Jiang, J. Self-sacrificial templating synthesis of porous quaternary Cu-Fe-Sn-S semiconductor nanotubes via microwave irradiation. *Nanotechnology* **2012**, *23*, 495601. [[CrossRef](#)] [[PubMed](#)]
38. Li, L.; Liu, X.Y.; Huang, J.; Cao, M.; Chen, S.Y.; Shen, Y.; Wang, L.J. Solution-based synthesis and characterization of $\text{Cu}_2\text{FeSnS}_4$ nanocrystals. *Mater. Chem. Phys.* **2012**, *133*, 688–691. [[CrossRef](#)]
39. Riha, S.C.; Parkinson, B.A.; Prieto, A.L. Solution-based synthesis and characterization of $\text{Cu}_2\text{ZnSnS}_4$ nanocrystals. *J. Am. Chem. Soc.* **2009**, *131*, 12054–12055. [[CrossRef](#)] [[PubMed](#)]

40. Lu, J.B.; Tang, Z.L.; Zhang, Z.T.; Shen, W. Preparation of LiFePO₄ with inverse opal structure and its satisfactory electrochemical properties. *Mater. Res. Bull.* **2005**, *40*, 2039–2046. [[CrossRef](#)]
41. Zhong, H.Z.; Zhou, Y.; Ye, M.F.; He, Y.J.; Ye, J.P.; He, C.; Yang, C.H.; Li, Y.F. Controlled synthesis and optical properties of colloidal ternary chalcogenide CuInS₂ nanocrystals. *Chem. Mater.* **2008**, *20*, 6434–6443. [[CrossRef](#)]
42. Jiang, X.; Xu, W.; Tan, R.Q.; Song, W.J.; Chen, J.M. Solvothermal synthesis of highly crystallized quaternary chalcogenide Cu₂FeSnS₄ particles. *Mater. Lett.* **2013**, *102*, 39–42. [[CrossRef](#)]
43. Wang, W.; Shen, H.L.; Yao, H.Y.; Li, J.Z. Preparation and properties of Cu₂FeSnS₄ nanocrystals by ultrasound-assisted microwave irradiation. *Mater. Lett.* **2014**, *125*, 183–186. [[CrossRef](#)]
44. Meng, X.K.; Deng, H.M.; Sun, L.; Yang, P.X.; Chu, J.H. Sulfurization temperature dependence of the structural transition in Cu₂FeSnS₄-based thin films. *Mater. Lett.* **2015**, *161*, 427–430. [[CrossRef](#)]
45. Kush, P.; Deori, K.; Kumar, A.; Deka, S. Efficient hydrogen/oxygen evolution and photocatalytic dye degradation and reduction of aqueous Cr(VI) by surfactant free hydrophilic Cu₂ZnSnS₄ nanoparticles. *J. Mater. Chem. A* **2015**, *3*, 8098–8106. [[CrossRef](#)]
46. Zhou, Z.H.; Zhang, P.G.; Lin, Y.L.; Ashalley, E.; Ji, H.N.; Wu, J.; Li, H.D.; Wang, Z.M. Microwave fabrication of Cu₂ZnSnS₄ nanoparticle and its visible light photocatalytic properties. *Nanoscale Res. Lett.* **2014**, *9*, 477. [[CrossRef](#)] [[PubMed](#)]
47. Ansari, M.Z.; Faraz, M.; Munjal, S.; Kumar, V.; Khare, N. Highly dispersible and uniform size Cu₂ZnSnS₄ nanoparticles for photocatalytic application. *Adv. Powder Technol.* **2017**, *28*, 2402–2409. [[CrossRef](#)]
48. Phaltane, S.A.; Vanalakar, S.A.; Bhat, T.S.; Patil, P.S.; Sartale, S.D.; Kadam, L.D. Photocatalytic degradation of methylene blue by hydrothermally synthesized CZTS nanoparticles. *J. Mater. Sci. Mater. Electron.* **2017**, *28*, 8186–8191. [[CrossRef](#)]



© 2017 by the authors. Licensee MDPI, Basel, Switzerland. This article is an open access article distributed under the terms and conditions of the Creative Commons Attribution (CC BY) license (<http://creativecommons.org/licenses/by/4.0/>).